

Surface Magnetism: Relativistic Effects at Semiconductor Interfaces and Solar Cells

U. Gerstmann, M. Rohrmüller, N.J. Vollmers, A. Konopka, S. Greulich-Weber, E. Rauls, M. Landmann, S. Sanna, A. Riefer, and W.G. Schmidt

Abstract Ab initio calculations of the electronic g -tensor of paramagnetic states at surfaces and solar cells are presented, whereby special emphasis is given onto the influence of relativistic effects. After discussing the numerical requirements for such calculations, we show that for silicon surfaces the g -tensor varies critically with the hydrogen coverage, and provides an exceptionally characteristic property. This holds also in the case of powder spectra where only the isotropic part g_{av} is available from experiments. Extending our calculations onto microcrystalline 3C-SiC, our study explains why sol-gel grown *undoped* material can serve as an excellent acceptor material for an effective charge separation in organic solar cells: Due to an auto-doping mechanism by surface-induced states it fits excellently into the energy level scheme of this kind of solar cell and has the potential to replace the usually used rather expensive fullerenes.

1 Introduction

Solar cells provide an increasing market with high potential for a further development. The global market for photovoltaics cells is expected to be doubled during the next decade. However, overcapacities will be an ongoing challenge for the manufacturers and a wedding-out and consolidation process seems to be unavoidable. One way out is the production of highly efficient solar cells by minimal costs. So far, however, such an optimization of the cells is mainly based on try and error. For a further improvement of cell performance a better understanding of the microscopic structures and the basic electronics behind the light-induced separation of charge carriers as well as the efficiency limiting processes is crucial.

U. Gerstmann · M. Rohrmüller · N.J. Vollmers · A. Konopka · S. Greulich-Weber · E. Rauls · M. Landmann · S. Sanna · A. Riefer · W.G. Schmidt (✉)
Lehrstuhl für Theoretische Physik, Universität Paderborn, 33095 Paderborn, Germany
e-mail: W.G.Schmidt@upb.de

Experimentally, electron paramagnetic resonance (EPR) provides a powerful tool to analyse the microscopic structure of paramagnetic systems. Since most of the electrically active centers in solar cells are those with unpaired electrons, these electronic states are paramagnetic. Hence, EPR provides an appropriate possibility to characterize the basic material as well as the solar cells itself. In many cases, however, the wealth of important information available from EPR measurements, cannot be extracted from experimental data alone. For an identification of the microscopic structures, accurate first principles calculations of as many as possible relevant properties are necessary to calculate a fingerprint of the structure that can be compared with the experimental values. From EPR experiments the components of the electronic g -tensor are available also in those cases in which hyperfine (hf) splittings cannot be resolved. However, in contrast to the *ab initio* calculation of hf splittings that already do have an appreciable history, quantitative predictions of electronic g -tensors making use of the machinery of *ab initio* density functional theory (DFT) have become possible only very recently [1]. In semiconductors, this has been already demonstrated successfully for defects in SiC and GaN bulk material [2–4]. For surfaces, however, theoretical data obtained by *first principle* calculation is very rare. In this work we show, that the EPR parameters are mainly influenced by relativistic effects like the spin-orbit coupling (SOC). At surfaces and interfaces these effects become exceptionally anisotropic giving rise to special effects like the so-called Rashba effect [5].

We evaluate our method using hydrogenated silicon surfaces as an example. Such surface states appear in hydrogenated microcrystalline silicon (μc -Si:H), a material that can be used for efficient and low-cost solar cells [6] (see Fig. 1).¹ We show that the *ab initio* calculation of g -tensors can help to elucidate the situation in such microcrystal. We calculate the elements of the electronic g -tensor for some paramagnetic states at silicon surfaces from first principles, using a recently developed gauge-including projector augmented plane wave (GI-PAW) approach [1, 9] in the framework of DFT. According to the in-diffusion of water and atmospheric gases [10] we investigate the EPR fingerprint of those paramagnetic states that are created by hydrogen adsorbed at Si(111) and Si(001) surfaces. Our approach is shown to be able to distinguish between different surface states [11]. For silicon surfaces with different hydrogen coverages, the g -tensor is by far more characteristic than the hf splitting of the Si dangling bonds or that of the adsorbed H atoms. This holds in cases of powder spectra like in the case of amorphous or microcrystalline material for solar cells where only the angular average of the spectra is available experimentally.

A central challenge on the way to optimized solar cells is to make the thickness of the individual layers smaller than the diffusion length of the charge carriers. Recently, 3C-SiC microcrystals grown by a sol-gel based process have been

¹In comparison with cells based on amorphous silicon suffer less from the notorious light-induced degradation, known as the Staebler-Wronski effect [7]. Best cell performance is, however, achieved for material grown close to the transition to amorphous growth [8].

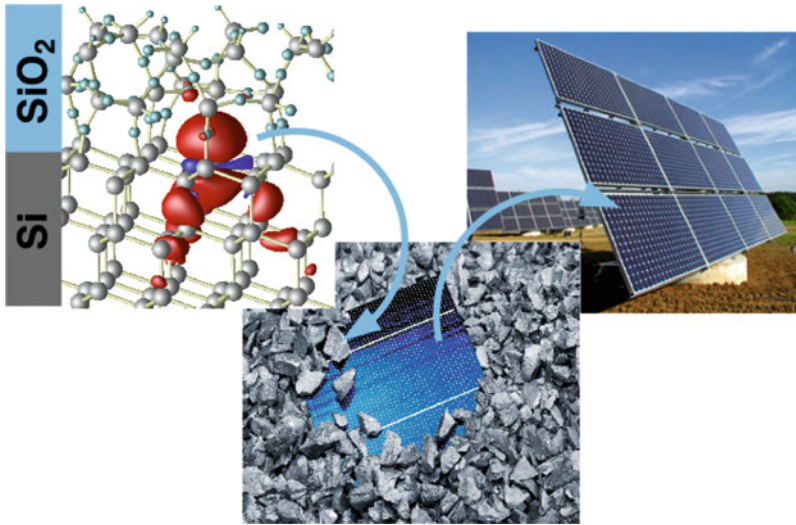


Fig. 1 From microcrystalline material (here: atomic structure of oxidized $\mu\text{c-Si}$) towards single solar cells and photovoltaic plantages

proposed as a promising acceptor material for photovoltaic applications [27]. Such $\mu\text{c-SiC}$ samples have been already characterized by optical spectroscopy and electron paramagnetic resonance (EPR) [32]. In this work, the available experimental data is analyzed with the help of *ab initio* DFT calculations resulting in electronic band structures and g -tensors. Based on this, a possible scenario for the observed acceptor process is discussed.

2 Methodology

Our first-principles calculations of the EPR parameters are based on density functional theory (DFT) using the generalized gradient approximation for the electron exchange and correlation functional (GGA-PBE) in its spin-polarized form [12]. The hyperfine splittings, i.e. the interaction of the magnetic moments of the electrons with those of the nuclei, are calculated taking into account relativistic effects in scalar-relativistic approximation [13, 14]. Although there exist a non-relativistic derivation for the isotropic contact interaction by Fermi [15], Breit has shown that the origin of the hyperfine splitting can be only described correctly in a relativistic treatment [16]. The static magnetic field caused by the magnetic moment $\boldsymbol{\mu}_{\mathbf{I}} = g_N \mu_N \mathbf{I}$ of a nucleus with gyromagnetic ratio g_N located at the origin is included using the vector potential for this magnetic field

$$\mathbf{A}_I(\mathbf{r}) = \nabla \times \left(\frac{\boldsymbol{\mu}_I}{r} \right) \quad (1)$$

replacing the momentum operator \mathbf{p} by the canonical momentum $\boldsymbol{\pi} = \mathbf{p} + e/c\mathbf{A}_I$ in Dirac's equation

$$(c\boldsymbol{\alpha} \cdot \boldsymbol{\pi} + \beta mc^2 + V - E_{rel}) \Psi = 0. \quad (2)$$

The influence of the resulting magnetic fields $\mathbf{B}_I(\mathbf{r}) = \nabla \times \mathbf{A}_I(\mathbf{r})$ leads to level splittings in the $10^{-12} \dots 10^{-2}$ eV range. The smallness of these splittings allows a simplified computation via perturbation theory. Within first order perturbation theory the expectation value of the hyperfine interaction is given by

$$E_{\text{HF}} = -e \langle \Psi | \boldsymbol{\alpha} \cdot \mathbf{A}_I(\mathbf{r}) | \Psi \rangle, \quad (3)$$

Here, $\boldsymbol{\alpha}$ is a 4×4 matrix constructed from the 2×2 Pauli spin matrices σ_x , σ_y , and σ_z , respectively, whereby $|\Psi\rangle = \begin{pmatrix} \Phi_L \\ \Phi_S \end{pmatrix}$, is given by the Dirac spinor decomposing into the two-component Pauli spinors Φ_L and Φ_S . For light atoms, Φ_L is the large component whereas Φ_S turns out to be small. This leads to

$$E_{\text{HF}} = -e (\langle \Phi_L | \boldsymbol{\sigma} \cdot \mathbf{A}(\mathbf{r}) | \Phi_S \rangle + \langle \Phi_S | \boldsymbol{\sigma} \cdot \mathbf{A}(\mathbf{r}) | \Phi_L \rangle). \quad (4)$$

Thus, E_{HF} is a genuine relativistic term that couples large and small components of Dirac's equation. The small component Φ_S can be expressed in terms of the large component Φ_L as

$$\Phi_S = \frac{c \boldsymbol{\sigma} \cdot \mathbf{p}}{2mc^2 + E - V(\mathbf{r})} \Phi_L = \frac{S(\mathbf{r})}{2mc^2} (\boldsymbol{\sigma} \cdot \mathbf{p}) \Phi_L, \quad (5)$$

whereby $S(r)$ is the inverse relativistic mass correction. This can be used to express Φ_S in terms of Φ_L , leading to expectation values containing the large component exclusively [17]. In the case of orbital quenching we obtain [14]:

$$E_{\text{contact}} = -\frac{8\pi}{3} \mu_B \langle \Phi_L | S(\mathbf{r}) \boldsymbol{\mu}_I \cdot \boldsymbol{\sigma} \delta(\mathbf{r}) | \Phi_L \rangle + \left\langle \Phi_L \left| \frac{1}{r^4} \frac{\partial S}{\partial r} [\boldsymbol{\mu}_I \cdot \boldsymbol{\sigma} r^2 - (\boldsymbol{\mu}_I \cdot \mathbf{r}) (\boldsymbol{\sigma} \cdot \mathbf{r})] \right| \Phi_L \right\rangle \quad (6)$$

$$E_{\text{dip}} = \mu_B \left\langle \Phi_L \left| \frac{1}{r^5} [\boldsymbol{\sigma} \cdot \boldsymbol{\mu}_I r^2 - 3 (\boldsymbol{\sigma} \cdot \mathbf{r}) (\boldsymbol{\mu}_I \cdot \mathbf{r})] \right| \Phi_L \right\rangle \quad (7)$$

The dipolar term E_{dip} is angular dependent and, thus, in the general case gives rise to anisotropic hf tensors. In the non-relativistic case, since $S(\mathbf{r}) \rightarrow 1$, only the first term in (6) contributes to the *isotropic* part, the so-called contact term. By this,

we obtain the results of the classical theory given by Fermi [15], that only the probability amplitude at the nucleus contributes. In the relativistic case, however, this first term does not contribute at all. It is second term in (6) which becomes the relativistic analogue to the contact interaction. For a pure Coulombic potential

$$V(r) = \frac{-Ze^2}{r} \quad (8)$$

the derivative $\partial S(r)/\partial r$ is similar to a broadened δ -function

$$\delta_{\text{Th}}(\mathbf{r}) = \frac{1}{4\pi r^2} \frac{\partial S}{\partial r} = \frac{1}{4\pi r^2} \frac{r_{\text{Th}}/2}{\left[\left(1 + \frac{E}{2mc^2} \right) r + r_{\text{Th}}/2 \right]^2}. \quad (9)$$

In other words, the magnetization density of the electron in the relativistic theory is not evaluated at the origin, where it would be divergent for s electrons, but is averaged over a sphere of radius

$$r_{\text{Th}} = \frac{Ze^2}{mc^2} \quad (10)$$

which is the Thomson radius, about ten times the nuclear radius.

As a result, the divergence of the s electrons presents no problem. Also if we approximate the nuclear potential by that of a charged volume rather than that of a point charge [18], the divergence already disappears. However, it is important to note, that we would obtain divergent contact terms mixing the approximations, e.g. using (scalar)² relativistic orbitals in a non-relativistic formula.

Whereas the hf splittings depend on the magnetization density $m(\mathbf{r}) = n^\uparrow(\mathbf{r}) - n^\downarrow(\mathbf{r})$ exclusively, the main deviation of the g -tensor from its free electron value $g_e \approx 2.002\ 319\ 278$ is given by the spin-orbit coupling of the many-particle system. In physically transparent form it can be written in terms of spin-polarised electron currents $\mathbf{j}_\uparrow^{(1),\mu}$ and $\mathbf{j}_\downarrow^{(1),\mu}$ induced by a unit magnetic field \mathbf{B}^μ applied along the direction μ :

$$\Delta g_{\mu\nu}^{\text{SO}} = \frac{\alpha}{2S} \left[\sum_{\sigma=\pm 1(\uparrow,\downarrow)} \sigma \int \nabla V_{\text{eff}}^\sigma \times \mathbf{j}_\sigma^{(1),\mu}(\mathbf{r}) d^3r \right]_\nu. \quad (11)$$

To obtain this result we start again from Dirac's equation and apply perturbation theory with respect to spin-orbit coupling and to an external magnetic field \mathbf{B} .

² In the scalar relativistic treatment Φ_L is calculated solving Dirac's equation but thereby ignoring spin-orbit interactions. This leaves the electron spin as a "good" quantum number. Already in a scalar relativistic treatment, s -like wave functions diverge at the nuclear site (if the nucleus is taken to be a point charge).

α is the fine structure constant, S the total spin given by the number of unpaired electrons times 1 s. $\nabla V_{\text{eff}}^\sigma$ denotes the gradient of the spin-polarized effective potential. Besides ground state quantities the evaluation of the g -tensor requires the calculation of the spin-currents $\mathbf{j}_\sigma^{(1),\mu}$ in linear magnetic response [9]:

$$\mathbf{j}_\sigma^{(1),\mu}(\mathbf{r}) = 2 \sum_o \text{Re} \left\langle \psi_{(0),o}^\sigma | \mathcal{J}^p \mathcal{G}^\sigma(\varepsilon_o) \mathcal{H}_{(1)} | \psi_{(0),o}^\sigma \right\rangle + \frac{\alpha}{2} n^\sigma(\mathbf{r}) \cdot \mathbf{B}^\mu \times \mathbf{r} \quad (12)$$

$\mathcal{J}^p = \frac{1}{2} \frac{\nabla}{i} |\mathbf{r}\rangle \langle \mathbf{r}| + c.c.$ denotes the current operator for vanishing magnetic field. $\mathcal{H}^{(1)} = \frac{\alpha}{2} \mathbf{L} \cdot \mathbf{B}^\mu$ describes the influence of the *uniform* magnetic field determining the perturbed wavefunctions $|\psi_{(1),o}^\sigma\rangle = \mathcal{G}^\sigma(\varepsilon_o) \mathcal{H}_{(1)} |\psi_{(0),o}^\sigma\rangle$ via Green's function of the unperturbed system

$$\mathcal{G}^\sigma(\varepsilon) = \sum_e \frac{|\psi_{(0),e}^\sigma\rangle \langle \psi_{(0),e}^\sigma|}{\varepsilon - \varepsilon_e^\sigma}, \quad (13)$$

whereby the sum runs over the *empty* orbitals e .

Strictly seen, the formalism so far presented ensures only a faithful description of the nuclear and two-electron spin-orbital coupling. According Ref. [1, 11] higher order contributions can be approximately taken into account via the *spin-other-orbit correction*, given by the screening $\mathbf{B}^{(1),\mu}(\mathbf{r})$ of the external magnetic field \mathbf{B}^μ by the induced currents as experienced by the magnetization density $m(\mathbf{r})$ of the unpaired electrons:

$$\Delta g_{\mu\nu}^{\text{SOO}} = \frac{g_e \alpha}{2S} \int \mathbf{e}_\nu \cdot \mathbf{B}^{(1),\mu}(\mathbf{r}) m(\mathbf{r}) d^3r. \quad (14)$$

In the case of the paramagnetic states at Si surfaces the contribution of the SOO term comes out to be very small (clearly below 10 ppm). In other words, the spin-other-orbit contributions do not contribute considerably to the g -values given in Tables 1–4.

For a modelling of the surfaces we use supercells and periodic boundary conditions. Hence, the explicit treatment of an external magnetic field \mathbf{B} has to be done in a gauge-invariant way in order to retain the translation invariance of the wavefunctions. Here, the gauge-including projector augmented plane wave (GI-PAW) approach satisfies this requirement and allows an ab initio calculation of the all-electron magnetic response using an efficient pseudopotential approach [1, 9]. The GI-PAW approach is implemented in the pwscf-code (QUANTUM-ESPRESSO package) [19] and has been already applied successfully to identify paramagnetic defect structures in SiC and GaN [2–4].

To model the semiconductor surfaces (silicon and SiC) at least eight atomic layers are treated in a supercell, whereby the lowest layer was saturated with H atoms. To ensure a well defined transition to bulk material, the atoms in the lowest three layers were kept on their ideal bulk positions. All other atoms were allowed to relax freely. To minimize the interaction of the periodic images of the surface, 10 Å vacuum is inserted. We use supercells containing up to 175 atoms and

Table 1 Largest hf splittings (MHz) of a H vacancy at Si(111):H surface as calculated by ab initio DFT. θ denotes the angle between the principal axis of the hf tensor and the surface normal. All hf splittings due to H atoms are below 2 MHz

	# nuclei	A_1	A_2	A_3	θ
Si_1	1	-220.0	-220.0	-414.9	0.0°
Si_2	3	1.4	0.0	-6.7	52.1°
Si_3	3	-26.5	-27.4	-42.8	0.4°
Si_4	3	-20.1	-20.4	-26.7	66.3°
Si_5	3	-7.5	-7.7	-10.4	10.0°

Table 2 k -point convergence of the g -values calculated for the H vacancy at Si(111):H surface. Given are the principal values g_i as well as the angular averaged value g_{av} . θ denotes the angle between the principal axis g_3 and the surface normal

k -point mesh	g_{av}	g_1	g_2	g_3	θ
Γ	2.010887	2.01250	2.01250	2.00766	0.0°
$2 \times 2 \times 1$	2.006393	2.00925	2.00925	2.00068	0.0°
$3 \times 3 \times 1$	2.006607	2.00939	2.00939	2.00104	0.0°
$4 \times 4 \times 1$	2.006630	2.00939	2.00939	2.00111	0.0°
$5 \times 5 \times 1$	2.006630	2.00939	2.00939	2.00111	0.0°
$6 \times 6 \times 1$	2.006630	2.00939	2.00939	2.00111	0.0°

Table 3 Comparison of the calculated g -tensors for a single adsorbed H-atom and for a nearly complete H-coverage of the Si(001) surface. For a better comparison with the calculated hf splittings (MHz) the calculated Δg -values are here given in ppm

	A_1	A_2	A_3	θ_{hf}	Δg_{av}	Δg_1	Δg_2	Δg_3	θ
(111): H saturated with H vacancy	-220	-220	-415	0°	4,309	7,070	7,070	-1,213	0.0°
(001): single adsorbed H atom	-189	-189	-373	18°	-2,149	-2,079	-219	-4,139	27.8°
(001): monohydride with H vacancy	-254	-2,554	-450	20°	2,941	5,841	3,431	-449	33.5°

Table 4 Analysis of 3C-SiC microcrystals: Calculated g -tensor values for different surface related defects visualized in Fig. 5. The value experimentally observed for a μc -SiC powder spectrum and the corresponding angular averaged theoretical values g_{av} are also given

	Defect	g_{av}	g_1	g_2	g_3
	<i>Exp.</i>	2.0073			
(a)	Si(001):H	2.00320	2.00187	2.00359	2.00415
(b)	C(001):H	2.00292	2.00245	2.00273	2.00357
(c)	Si(001) + H	2.00268	2.00238	2.00271	2.00294
(d)	C(001) + N_C	2.00271	2.00180	2.00299	2.00333

norm-conserving pseudopotentials with a plane wave energy cutoff of 30 and 50 Ry for silicon and SiC, respectively. The ab initio calculation of the g -tensor is still very time-consuming: Whereas for the geometry optimisation a $2 \times 2 \times 1$ Monkhorst-Pack (MP) [20] k -point set comes out to be sufficient, to obtain converged estimates for the g -tensor in the general case $4 \times 4 \times 1$ samplings come out to be unavoidable. In some cases the number of k -points can be reduced by symmetry, but the number of $(k+q)$ -points has to be multiplied by a factor of 7 in order to obtain the derivatives in

the reciprocal space. A second requirement for the calculation of the spin-currents in linear magnetic response [9] is calculation of the Green's function (see Eq. 14). As a result, the calculation of a g -tensor becomes computationally extremely demanding and takes about an order of magnitude more CPU time than structure optimization. On the other hand, the calculation of the hyperfine splittings can be done on the fly. Given that structure optimization takes 1 day CPU time, and the g -tensor more than 10 days, the hf splittings are already available after 10 CPU minutes.

3 Results

We first discuss the H vacancy at a Si(111):H surface as a reference system. This structure is obtained if removing one H-atom from an otherwise completely hydrogenated Si(111) surface. It provides a simple model for a single paramagnetic dangling bond. Figure 2 shows several views of the microscopic structure and the corresponding magnetisation density $m(\mathbf{r})$. As can be seen from the top view (*lower left corner*), the structure shows perfect C_{3v} symmetry with the symmetry axis along the surface normal. An analysis of $m(\mathbf{r})$ at the nuclei leads to the hyperfine splittings given in Table 1. As intuitively expected, the by far largest hf splitting (-415 and -220 MHz for the magnetic field along and perpendicular to the surface normal, respectively) is due to the unsaturated Si-atom at the surface. The right part of Fig. 2 shows the magnetization density in a plane parallel to the surface normal. It can be considered as a typical 'textbook' fingerprint of a dangling bond. As an additional feature, weaker accumulations of $m(\mathbf{r})$ are found along the Si zig-zag line. As a result, besides that of the dangling bond nucleus itself, our ab initio calculations predict further characteristic hf splitting. With a value of about -43 MHz due to three equivalent nuclei Si_3 in the third layer, the hf splitting could be large enough to be resolved in EPR measurements. In contrast, the hf splittings below 10 MHz (see Table 1), especially that of the H atoms at the Si(111) surface (below 2 MHz) are too small to be resolved. They will contribute to the width of the central line instead. The position of this central line is determined by the g -tensor.

In Table 2, the calculated principal g -values are compiled for different k -point samplings. At least for the $4 \times 4 \times 1$ and larger samplings the values can be considered converged. The vanishing angle θ between g_3 and the surface normal confirms again the perfect alignment of the dangling bond along the surface normal. Perpendicular to the surface normal with $g_1 = g_2 = 2.00939$ comparatively large g -values are predicted. The g -value parallel to the surface normal remains similar to that of the free electron. The reason for this particular anisotropic shape is the perfect alignment of the dangling bond along the surface normal resulting in a strongly anisotropic spin-orbit coupling similar to the Rashba-type [5] characterized by vanishing spin-orbit coupling for the spin along the surface normal.

We also take this textbook dangling bond as an example to evaluate the computational efficiency of our code in massive parallel application. We analyse the hydrogen vacancy at the H-terminated Si(111):H surface in a 119 atom supercell by

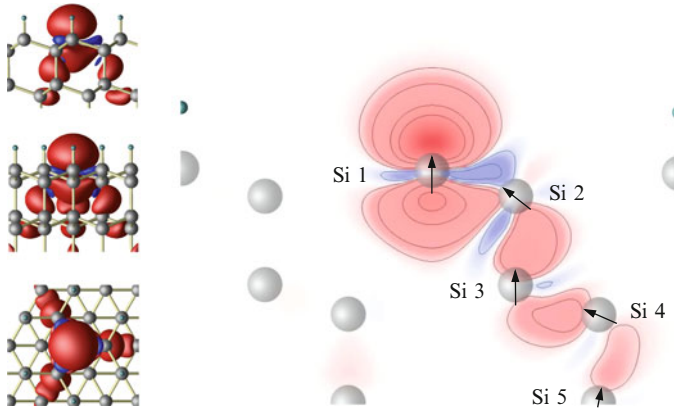


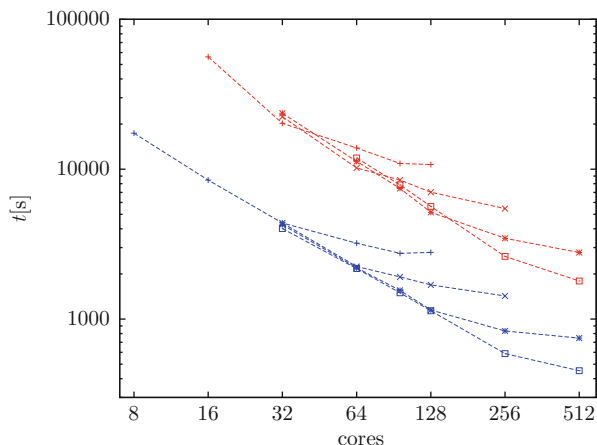
Fig. 2 Microscopic structure and magnetisation density of the paramagnetic H vacancy at Si(111):H surface for different side views (*lower left corner*: top view). Plot of the magnetisation density within a plane including the surface normal. The *arrows* describe the direction of the magnetization density (i.e. the principal axis of the hf tensor) at the Si-nuclei

using a $6 \times 6 \times 1$ k -point set. Due to the trigonal C_{3v} symmetry this results in an explicit treatment of 24 k -points. In the standard mode, the QUANTUM-ESPRESSO code uses parallelization with respect to reciprocal lattice vectors. For Fast Fourier Transformations (FFT) and a limited number of processors, already this simple treatment often provides a good scaling with the number of quasi-processors (cores) used. However, especially in cases where the number of lattice vectors does not fit to the number of cores and for more than 32 cores the performance of the calculations becomes more and more saturated (see Fig. 3). We cannot exclude that the observed saturation is also supported by additional communication between the several nodes as unavoidable for $N_{cores} > 32$. However, for band structure calculations, in general for calculation with a large number of k -points³ a second parallelization via pools can be established. Here, the k -points are divided into pools whereby each pool contains a subset of the k -points. By this, for the present architecture we obtain linear scaling for up to 256 processors (16 nodes).

The number of pools is obvious limited by the number of k -points in the calculation and more critical by the memory consumption per core: By doubling the number of pools the required memory per core is increased by a factor of 1.2–1.4. The best scaling, however, is obtained for metallic systems with several thousands of k -points. On the other hand, for a small number of cores per pool the parallelization via k -points can become counter-productive. For a given system size (including cell size, number of electrons/bands, number of k -points) and for a chosen number of cores an optimal number of pools exists, mostly larger than the available memory allows. In other words, the overall limiting factor is given by the memory available

³For spin-polarized calculations, the second spin channel is realized by doubling the k -point set.

Fig. 3 CPU time on the HLRS CRAY XE6 for a self-consistent field calculations (blue) and g -tensor calculations (red). For exact description of the used parameters see text. The number of pools is marked by the symbols plus, cross, star, square corresponding to 1, 2, 4 and 8 pools, respectively



per core. Here, for future work, especially for larger systems with up to thousand atoms, an architecture with more than 2 GB RAM per core would be desirable.

Coming back to the physical results of our calculations, the situation becomes more difficult in case of the Si(001) surface that has an appreciable history of both experimental and theoretical work (see e.g. Ref. [21] for a review). It shows the famous 2×1 reconstruction into rows of buckling Si dimers. The left part of Fig. 4 shows a side view along these dimer rows. The adsorption of a single H atom breaks the double bond of a dimer. The result is a single dangling bond (left row but one in Fig. 4). If further H atoms are adsorbed at the Si(001) surface, either further dimers are broken or existing dangling bonds are saturated. In the case of complete saturation, each Si atom at the surface bonds one H atom. In Table 3, the EPR parameters for such microstructures are compared. Obviously, the g -tensor varies strongly with the hydrogen coverage. Especially the Δg_3 -values along the principal axis of the g -tensor differ by more than one order of magnitude. In this sense, the g -tensor is by far more characteristic than the hf splittings which vary only within 20%. Since in contrast to the hf splittings the sign of Δg can be determined experimentally, this holds also in case of powder spectra where only the isotropic part g_{av} is available from experiment.

The results and experiences obtained for the H-terminated silicon surfaces gives us confidence that our method will be accurate enough to predict the spectroscopic magnetic properties of dangling bonds in real devices, like solar cells based on microcrystalline SiC:

Microcrystalline silicon carbide ($\mu\text{c-SiC}$) has become an attractive new class of advanced materials for light emitting diodes and heterojunction photovoltaic devices [24]. Here, the microcrystallites are of interest as effective charge carrier collectors in organic solar cells. When a photon is absorbed by an organic photoactive material, an exciton, i.e., a bound state of an electron and a hole, is created. Due to the notably short exciton lifetime of several tens of nanoseconds, the most important design criterion for such solar cells is to make the thickness

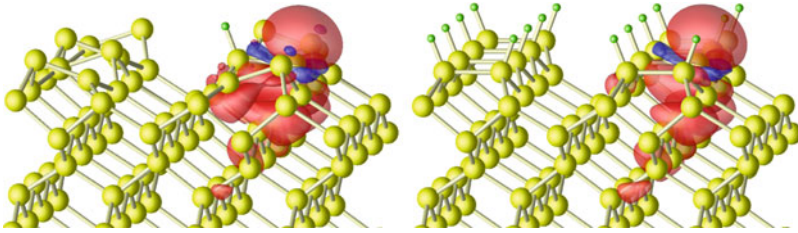


Fig. 4 Structure and magnetisation densities for a single adsorbed H-atom (*left*) and for a nearly complete H-coverage of the Si(001) surface (H vacancy at monohydride surface, *right*)

of the individual layers smaller than the diffusion length of the exciton [22, 23]. For this purpose, usually fullerene molecules are dispersed in a polymer matrix. One possibility to further increase the efficiency of this kind of solar cells is to use alternative acceptor materials with a more suitable position of the LUMO (lowest unoccupied molecular orbital) level. By adjusting the latter, the open circuit voltage of the solar cell can be increased at the expense of the energy lost by the electrons connected with charge transfer from donor to acceptor material. Instead of using rather expensive fullerenes, currently wide bandgap micro- and nano-crystals as acceptor materials are under discussion, such as TiO_2 [25], ZnO [26], and last but not least SiC [27].

Usually, the mentioned materials provide unavoidable technical difficulties, such as intrinsic defects, the lack of suitable *p*-doping [28] or omnipresent *n*-doping. As an promising alternative, in Ref. [31] a sol-gel growth process for $\mu\text{c-SiC}$ has been proposed. The resulting material is almost free from usually unavoidable nitrogen donors, allowing arbitrary doping. In Ref. [32] electron paramagnetic resonance (EPR) was used as an analytic tool for the control of the doping success: Doping with N, Al, and P leads to different, characteristic EPR spectra. They are clearly different from those known for usual shallow donors and acceptors in bulk SiC . The nominally undoped and nitrogen-doped samples show an EPR line similar to a center discovered in porous 3C-SiC, assigned to a carbon dangling bond at the 3C-SiC/ SiO_2 interface. The *g*-factor is slightly different, but the line half width is almost the same. At first view, this similarity is very surprising since the microcrystallites are not oxidized: Even if the crystals became as large as $20\ \mu\text{m}$ in diameter, they do not show the typical SiO_2 lines in nuclear magnetic resonance and infrared reflection spectroscopy. Electrical and photoluminescence measurements support the finding that the required acceptor behavior of $\mu\text{c-SiC}$ is caused by surface-related defects in combination with an appropriate position of the Fermi level, which is determined by doping.

Based on the experimental results, the microscopic structure of the responsible defect structure at the clean surface of the micro-crystallites and its influence onto the charge-separation mechanism is discussed with the help of *ab initio* calculations. In order to elucidate the microscopic origin of the observed EPR signals, we calculate the EPR parameters for some possible dangling-bond related structures

and compare them with the experimental values. For a modelling of the surfaces we use the settings already mentioned in connection with the partially hydrogenated silicon surfaces. In close analogy to the (001)-oriented silicon surfaces we first discuss the different defects at the corresponding surface of 3C-SiC (see Fig. 5). In silicon, the clean (001) surface is stabilized by rows of buckled dimers, which are still surviving if the surface is partially hydrogenated. Only, if nearly all silicon atoms are mono-hydrogenated, the dimers at the reconstructed surface lose their buckling. In 3C-SiC, the silicon-terminated Si-surface looks similar at first view. But due to the smaller bond length in SiC the buckling becomes less efficient, resulting in almost all cases in surfaces with very complicated reconstructions [29, 30] showing metallic and diamagnetic properties. Hence, these configurations cannot be responsible for the observed paramagnetic structures.

Only an almost completely hydrogen-passivated configuration with one missing hydrogen (shown in Fig. 5a) leads to a paramagnetic surface state. In the following, we focus onto the carbon-terminated C-surface, where the situation is by far more straightforward. Here, similar to the case of diamond, already the clean surface provides a 2×1 dimer reconstruction without buckling (see also Fig. 5b–d). All these surface related defects provide paramagnetic states and are, thus, possible candidates to explain the $g = 2.0073$ EPR-signal of unknown origin. In Table 4, the calculated elements of the corresponding g -tensor are listed. Since no angular dependent EPR-measurements for the microcrystalline SiC-powder were possible, the only value that has to be compared to the experiment is g_{av} , the average g -value over possible orientations. In all cases, Si-related hyperfine splittings in the range 20–30 MHz can be found, but the calculated average g -values g_{av} are far away from the experimental data. So, the corresponding models have to be discarded as explanation for the surface related EPR-signal.

Nevertheless, it is worth to check the energetic level of the surface related defects. For this, we have to analyse the corresponding electronic band structures. Figure 6 (*middle*) shows the band structure of the clean C-terminated (001) surface, calculated using the gradient-corrected PBE functional. In comparison with the SiC-bulk material (*left part*) additional broad bands appear in the gap. Those in the lower part are occupied covering a 1.2 eV broad region. The unoccupied bands overlap with the conduction bands of the bulk material, so that the position of the LUMO is lowered. In total, the fundamental gap is considerably reduced to 0.2 eV. Having in mind the well-known underestimation of band gaps by the local density approximation (LDA) or the gradient-corrected functionals like PBE (e.g. the fundamental gap comes out about 1.4 eV while the experimental value is 2.4 eV for 3C-SiC), the experimental values should be larger. To determine the exact positions of the band edges further elaborated calculations (e.g. hybrid functionals) would be necessary. Nevertheless, the LDA prediction of the gap considerably reduced from both the valence band as well as from the conduction band can be considered at least qualitatively correct. The result is something like an auto-doping of the 3C-SiC microcrystals. The additional unpaired electron, introduced by a paramagnetic surface structure, leads only to an additional energy level clearly below the highest occupied surface state, but leaves all other features of the band structure

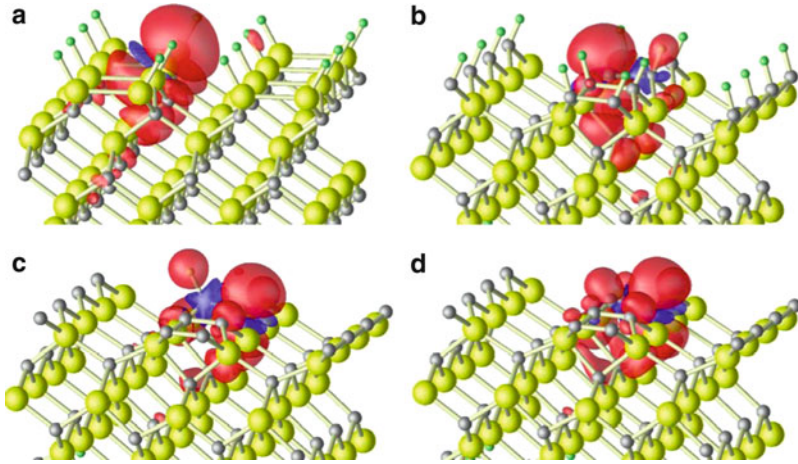


Fig. 5 Magnetization density of different surface-defects at the (001) surface of 3C-SiC. (a) Si-terminated surface, hydrogen passivated but with one missing H-atom Si(001)-H, (b) the corresponding defect at the C-terminated surface C(001)-H, (c) C-terminated surface with one H-atom adsorbed C(001)+H, (d) C-terminated surface with a substitutinal nitrogen atom on a C-site C(001)+N_C

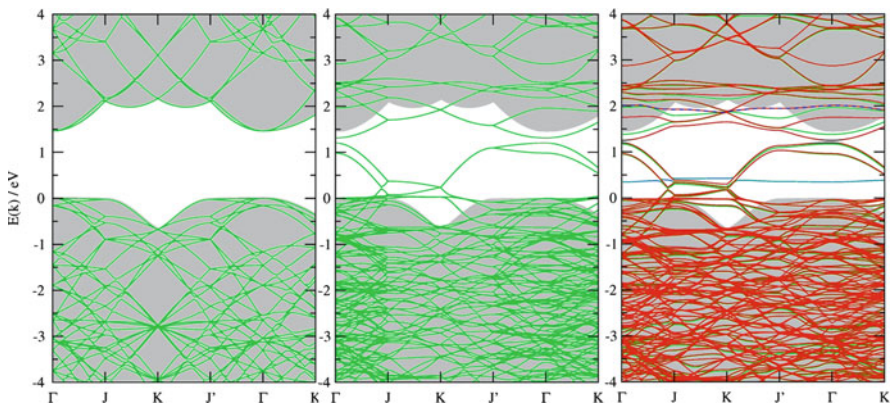


Fig. 6 Calculated band structure of 3C-SiC bulk (*left*) and for a 2×1 dimer-reconstructed SiC (001) C-surface (*middle*). The remarkable reduction of the fundamental gap (*shaded grey*) by the surface leads to an efficient auto-doping. Additional localized defects at the surface (*right*) induce additional defect levels (*blue*) and give rise to a spin-polarized band structure, but do not change the situation with respect to the LUMO considerably

of the clean surface unchanged. In all cases, the gap is significantly reduced, and the pure existence of the surface leads to an efficient auto-doping. In other words, independent from details of the paramagnetic defect structure, already the nominally undoped micro-crystalline sol-gel 3C-SiC behaves as an efficient acceptor for the charge carriers collection.

4 Conclusions

Ab initio calculations of the electronic g -tensor of paramagnetic states at surfaces and solar cells are presented. After discussing the numerical requirements for such calculations, we show that for silicon surfaces the g -tensor varies critically with the hydrogen coverage, and is by far more characteristic than the hf splitting of the Si dangling bonds or the adsorbed H atoms. This holds also in the case of powder spectra where only the isotropic part g_{av} is available from experiments. Extending our calculations onto micro- and nano-crystalline 3C-SiC as a basic material for solar cells, our study shows that sol-gel grown material can serve as an excellent acceptor material for an effective charge separation in organic solar cells. It fits excellently into the energy level scheme of this kind of solar cell and has the potential to replace the usually used, rather expensive fullerenes. It turned out, that already undoped μc -3C-SiC acts as a particular suitable acceptor due to its auto-doping mechanism by a surface-induced band structure.

Acknowledgements We gratefully acknowledge financial support from the DFG as well as supercomputer time provided by the HLRS Stuttgart and the Paderborn PC².

References

1. Ch.J. Pickard and F. Mauri, Phys. Rev. Lett. **88**, 086403 (2002).
2. U. Gerstmann, E. Rauls, S. Greulich-Weber, E.N. Kalabukhova, D.V. Savchenko, A. Pöpl, and F. Mauri, Mat. Sci. Forum **556–557**, 391 (2006).
3. U. Gerstmann, A.P. Seitsonen, F. Mauri, and J. von Bardeleben, Mat. Sci. Forum **615–617**, 357 (2009).
4. U. Gerstmann, A.P. Seitsonen, and F. Mauri, phys. stat. sol. (b) **245**, 924 (2008).
5. E.I. Rashba, Fiz. Tverdogo Tela **2**, 1224 (1960); Sov. Phys. Solid State **2**, 1109 (1960).
6. E. Vallet-Sauvain, U. Kroll, J. Meier, A. Sah, and J. Pohl, J. Appl. Phys. **87**, 3137 (2000).
7. D.L. Staebler, C.R. Wronski, Appl. Phys. Lett. **31**, 292 (1977).
8. S. Klein, F. Finger, R. Carius, T.Dylla, B. Rech, M. Grimm, L. Houben, and M. Stutzmann, Thin Solid Films **430**, 202, (2003).
9. Ch.J. Pickard and F. Mauri, Phys. Rev. B **63**, 245101 (2001).
10. F. Finger, R. Carius, T. Dylla, S. Klein, S. Okur, and M. Günes, IEE Proc.-Circuits Devices Syst. **150**, 309 (2003).
11. U. Gerstmann, M. Rohrmüller, F. Mauri, and W.G. Schmidt, phys. stat. sol. (c) **7**, 157 (2010).
12. J. P. Perdew, K. Burke, and M. Ernzerhof, Phys. Rev. Lett. **78**, 1396 (1997).
13. P.E. Blöchl, Phys. Rev. B **62**, 6158 (2000).
14. U. Gerstmann, phys. stat. solidi (b) **248**, 1319 (2011); p. 305–339 in “*Advanced Calculations for Defects in Materials*” edited by A. Alkauskas, P. Deák, J. Neugebauer, A. Pasquarello, and C.G. Van de Walle, Wiley-VCH, Weinheim, 2011.
15. E. Fermi, Z. Phys. **60**, 320 (1930).
16. G. Breit, Phys. Rev. **35**, 1447 (1930).
17. S. Blügel, H. Akai, R. Zeller, P.H. Dederichs, Phys. Rev. B. **35**, 3271 (1987).
18. H.A. Bethe, J.W. Negele, Nucl. Phys. A **117**, 575 (1968).
19. P. Giannozzi et al., J. Phys.: Condens. Matter **21**, 395502 (2009); <http://www.quantum-espresso.org>.

20. H.J. Monkhorst and J.D. Pack, Phys. Rev. B **13**, 5188 (1976).
21. J. Dabrowski in *Silicon Surfaces and Formation of Interfaces* ed. by J. Dabrowski and H.J. Müssig, p. 82–204 (World Scientific, Singapore 2000).
22. N.S. Saricifti, L. Smilowitz, A.J. Heeger, F. Wudl, Science **258**, 1474 (1992).
23. C.J. Brabec, G. Zerza, G. Cerullo, S. De Silvestri, S. Luzatti, J.C. Hummelen, N.S. Saricifti, Chem. Phys. Lett. **340**, 232 (2001).
24. G. Yu, J. Gao, J.C. Hummelen, F. Wudl, A.J. Heeger, Science **270**, 1789 (1995).
25. Q. Fan, B. McQuillin, D.D.C. Bradley, S. Whitelegg, A.B. Seddon, Chem. Phys. Lett. **347**, 325–330 (2001).
26. J.J. Cole, X. Wang, R.J. Knuesel, and H.O. Jacobs, Nano Lett. **8**, 1477–1481 (2008).
27. S. Ogawa, Appl. Phys. **46**, 518–522 (2007).
28. N. T. Son, Mt. Wagner, C. G. Hemmingsson, L. Storasta, B. Magnusson, W. M. Chen, S. Greulich-Weber, J. -M. Spaeth, and E. Janzen, in *Silicon Carbide, Recent Major Advances*, Eds. W. J. Choyke, H. Matsunami, G. Pensel, Springer Berlin, Heidelberg 2004, 461–492, ISBN 3-540-40458-9.
29. V. Yu. Aristov, phys. usp. **44**, 761 (2001).
30. Wenchang Lu, W.G. Schmidt, E.L. Briggs, and J. Bernholc, Phys. Rev. Lett. **85**, 4381–4384 (2000).
31. B. Friedel, S. Greulich-Weber, Mater. Res. Soc. Symp. Proc. **963**, 0963-Q15-10, Materials Research Society (2007).
32. A. Konopka, S. Greulich-Weber, E. Rauls, W.G. Schmidt, and U. Gerstmann, Mater. Res. Soc. Symp. Proc. **1322**, mrss11-1322-b10-02 (2011).